

Calibration of a deformable mirror and Strehl ratio measurements by use of phase diversity

Mats G. Löfdahl, Göran B. Scharmer, and Wang Wei

Calibration experiments with a bimorph mirror are presented. Phase-diversity wave-front sensing is used for measuring the control matrix, nulling wave-front errors in the optical setup, including the mirror, and measuring Strehl ratios and residual higher-order aberrations. The Strehl ratio of the calibrated system is measured to be 0.975, corresponding to 1/40 wave rms in the residual wave front. The conclusion is that a phase-diversity wave-front sensor is easier to install and use than interferometers and can replace them in optical setups for testing adaptive optics systems. © 2000 Optical Society of America

OCIS codes: 010.7350, 010.1080, 120.6650, 110.3000, 110.6770.

1. Introduction

The 50-cm Swedish Vacuum Solar Telescope¹ is designed for high-resolution observations of the solar photosphere. With its simple but high-quality optics and location at an excellent site, it frequently produces diffraction-limited images. To achieve this resolution at a high percentile, a number of real-time techniques, such as automatic frame selection, tip-tilt correction, and automatic focusing,^{2,3} can be used. Residual aberrations are corrected by postcollection wave-front sensing and image restoration with phase diversity^{4,5} (PD). We recently installed an adaptive optics (AO) system to improve performance further and to gain experience for the upcoming upgrade of the telescope to a 97-cm aperture.⁶ Inclusion of AO will be necessary for this telescope to perform near its diffraction limit in the visible.

An important part of any AO system is the ability cancel to any wave-front errors in the optics and to measure the control matrix that maps changes in wave front to changes in the control voltages of the mirror. The current real-time AO system wave-front sensor (WFS) in use in our system is a Shack-Hartmann (SH) WFS, described in a separate paper.⁷ In implementing such a WFS it is important to have

a means to measure independently the quality of the wave-front and the control matrix, including higher-order aberrations that cannot be measured with the SH WFS. Usually this is done with an interferometer. In this paper we describe laboratory experiments performed instead with a PD WFS installed in a path parallel to that of the SH WFS.

PD methods and algorithms have been described by several authors^{4,8-12} since the concept was proposed in 1979.¹³ They belong to a class of wave-front sensing and image reconstruction methods that use modeling of the image creation process to estimate the most likely model parameters from multiple measurements of the same object.^{14,15} They offer several important advantages compared with many other WFS methods. Extended objects, such as the solar surface, can be used. The WFS is in the image plane of the science camera, which combines wave-front sensing with estimates of the object, making it possible to restore the observed images. PD methods and algorithms also estimate the wave fronts directly, rather than local gradients that have to be fitted to wave fronts. When they are used with a pointlike source, direct measurements of the Strehl ratio (SR) are possible, providing verification of the measured wave-front rms. In PD, information about the phase and the object is extracted from at least two images, where the same object is encoded with a known difference in phase between the two imaging channels. The PD between the two channels that is commonly used is quadratic in the radial pupil plane coordinate, because it can easily be realized by addition of a few millimeters to the optical path, e.g., with a beam splitter or (if seeing is negli-

The authors are with the Royal Swedish Academy of Sciences, Stockholm Observatory, SE-133 36 Saltsjöbaden, Sweden. M. G. Löfdahl's e-mail address is mats@astro.su.se.

Received 27 July 1999; revised manuscript received 18 October 1999.

0003-6935/00/010094-10\$15.00/0

© 2000 Optical Society of America

gible) even by refocusing of the camera between consecutive exposures. Thus, little extra optics is required.

Laboratory experiments have demonstrated that PD is a practical tool for estimating and correcting the phase errors of segmented mirrors, deformable mirrors, and liquid-crystal spatial light modulators.^{10,16} The seeing conditions under which it is possible to sense the pistons of the individual segments of the 10-m Keck primary mirror were recently explored.¹⁷ A variation on the PD concept was used at the Starfire optical range to estimate fixed aberration differences between a SH WFS and an imaging path.¹⁸ However, we are not aware of any previous experiments in which PD measurements were used to measure the control matrix of the phase-changing element.

This paper is organized as follows: We introduce the concept of the PD WFS in Section 2, and we describe the deformable mirror and our optical setup in Section 3. In Section 4 we describe our procedure for measuring the control matrix of the deformable mirror by using PD, and in Section 5 we describe the use of this control matrix together with a PD WFS in a closed loop to calibrate the mirror. The results of the calibration are verified with PD-assisted Strehl ratio measurements in Section 6. We end with some conclusions in Section 7.

2. Phase Diversity

We refer to Ref. 4 for details of the PD algorithm used for wave-front sensing. This short overview introduces the notion required for the analysis in this paper.

The data that is used to sense one wave front are two simultaneous, dark-current-corrected images g_k of the same object f , with a known difference in focus. The focus difference means that the data have diversity in the pupil plane phase ϕ , also known as the wave front. With the convention that $k = 0$ for the conventional, in-focus channel and $k = 1$ for the diversity, out-of-focus channel, the images are modeled as

$$g_k(x) = f(x) * s_k(x) + n_k(x) = \mathcal{F}^{-1}\{F(u)S_k(u) + N_k(u)\}, \quad (1)$$

where s_k is the point-spread function, n_k is an additive Gaussian noise term, and $*$ is the convolution operator. \mathcal{F}^{-1} is the inverse Fourier transform, and capital letters are used for transforms of lowercase function symbols, so S_k is the optical transfer function. The two-dimensional spatial and spatial-frequency coordinates, respectively, x and u , will be suppressed from here on. The wave front is modeled as an expansion in basis functions ψ_j :

$$\phi = \sum_j \alpha_j \psi_j. \quad (2)$$

The basis functions used here are Zernike polynomials Z_m , as defined in Ref. 19, but, for ease of notation when some modes are excluded, we lexicographically

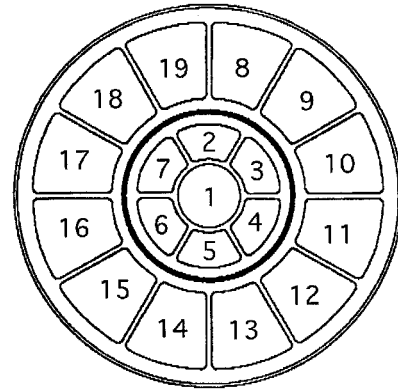


Fig. 1. Electrode configuration of the bimorph mirror. The thick circle inside the outer ring of electrodes indicates the 34-mm diameter of the active area. Courtesy of Laplacian Optics, Inc.

arrange whatever Zernike modes are included in an unbroken sequence. The coefficients will sometimes be written as a column vector, $\alpha = [\alpha_1, \dots, \alpha_J]^T$.

We find the maximum-likelihood estimates of f and α by minimizing an error metric, L , measuring the consistency of the estimates with the data. Using a circumflex to denote PD estimates of a function, we can write the metric as

$$L = \sum_x [|g_0 - \hat{g}_0(\alpha, D)|^2 + |g_1 - \hat{g}_1(\alpha, D)|^2], \quad (3)$$

where D is the assumed pupil diameter and

$$\hat{g}_k(\alpha, D) = \mathcal{F}^{-1}\{\hat{F}(\alpha, D)\hat{S}_k(\alpha, D)\}. \quad (4)$$

The object estimate can be written as

$$\hat{F} = H \frac{G_0 \hat{S}_0 + G_1 \hat{S}_1}{|\hat{S}_0|^2 + |\hat{S}_1|^2}, \quad (5)$$

where H is a low-pass filter that is usually optimized with respect to the signal-to-noise ratio.

The nonlinear minimization problem is linearized, which leads to an iterative scheme in which systems of equations have to be solved. We use the singular-value (SV) method to solve equation systems.^{20,21} The iterations proceed until a convergence criterion is reached. Here, we terminate the iterations when the rms of the wave-front change is less than 10^{-3} rad from one iteration to the next.

It should be noted that PD works on extended objects, even objects that extend outside of the field of view. Pointlike sources give a better signal-to-noise ratio at high spatial frequencies, which is of importance particularly with poor detector modulation transfer functions (MTF's) at high frequencies.

3. Deformable Mirror and Optics Setup

The 19-electrode bimorph mirror was constructed by Laplacian Optics, Inc. The electrode pattern shown in Fig. 1 is deposited upon each of two thin, sandwiched plates of piezoelectric material that are glued to the mirror. Voltage applied to an electrode locally

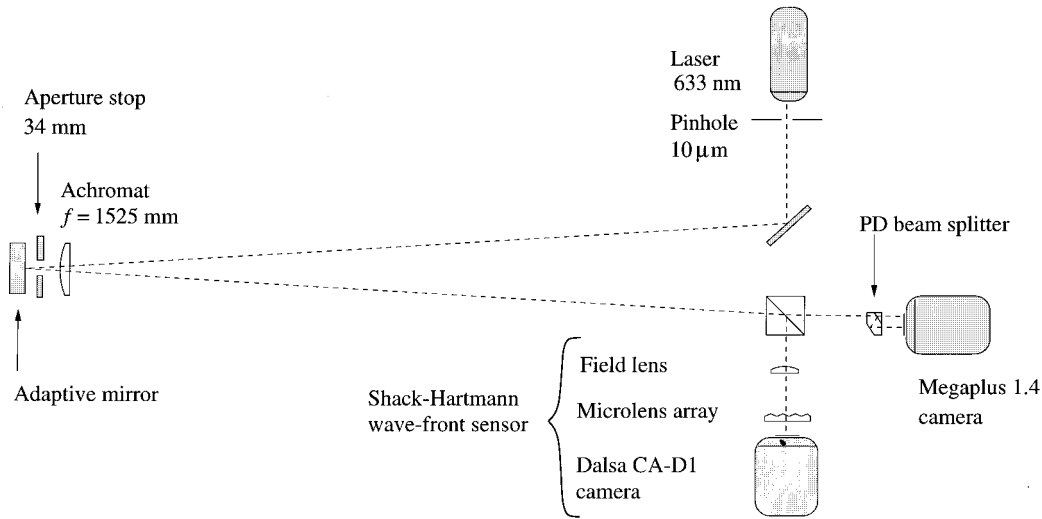


Fig. 2. Optical setup.

expands one of the plates and contracts the other, which makes the bimorph bend. The mirror is designed primarily to correct for Karhunen–Loeve polynomials 2–15, which are similar to the corresponding Zernike polynomials. These modes are defined within a 34-mm diameter represented by the thick circle between the inner and outer rings of electrodes. The seven inner electrodes introduce wave-front curvature and tilt within this active area, whereas the outer twelve electrodes produce mainly wave-front tilt near the edge. Laplacian optics specifies that by using 19 channels it should be possible to flatten the mirror to better than $\lambda/10$, peak-to-valley (PTV) in the wave front.²²

The optical setup is shown in Fig. 2. An $f = 1525$ mm lens directly in front of the mirror was used in autocollimation. A 633-nm laser was pointed at an angle toward the center of the mirror through a 10- μm pinhole at the first lens focus. The pinhole serves the double purpose of providing an almost unresolved point source and giving a diffraction pattern that illuminates the pupil uniformly. In the Fraunhofer approximation, the diameter of the first dark ring in the Airy pattern is $d = 1.22\lambda z/w \approx 236$ mm $\gg 34$ mm, where w is the radius of the pinhole and z is the distance from the lens.

At the reflected focus we placed an Eastman Kodak Megapplus 1.4 camera with a KAF 1400 CCD (6.8 μm , 100% fill pixels) equipped with a beam splitter–prism arrangement that put one image in focus on the CCD together with a second image defocused by 8.5 mm along the optical axis, or 0.87 wave PTV of quadratic phase at $\lambda = 633$ nm. Experiments with the SH WFS are described in a separate paper.⁷

The provisional mask between the achromatic lens and the mirror, which provides an aperture stop, was cut by hand from a sheet of tin. During the calibration experiment the mirror was assumed to be circular with a diameter $D = 34$ mm, although measurements later showed that it is smaller and

slightly irregularly shaped. Using a digital vernier caliper, we made six evenly distributed measurements of the diameter, with a mean value of 33.4 mm. The standard deviation is 0.2 mm, which is a combination of measurement errors and irregularities in shape. See the discussion in Section 6 below.

4. Control-Matrix Measurement

The mathematical treatment used is similar to earlier approaches; see, e.g., Ref. 23. In a first step we approximately characterize the mapping between electrode voltages and the Zernike coefficients. We try to find the control matrix \mathbf{C} that gives us the P -element ($P = 19$ is the number of electrodes) column vector of voltages \mathbf{h} from a vector of wave-front coefficients $\boldsymbol{\alpha}$ through

$$\mathbf{h} = \mathbf{C}\boldsymbol{\alpha} = \sum_j^J \alpha_j \mathbf{v}_j. \quad (6)$$

\mathbf{v}_j are the column vectors of \mathbf{C} and the voltages that correspond to unit Zernike modes; cf. the wave-front expansion in Eq. (2). The control matrix can be written as the pseudoinverse of a matrix \mathbf{M} :

$$\mathbf{C} = (\mathbf{M}^T \mathbf{M})^{-1} \mathbf{M}^T, \quad (7)$$

where \mathbf{M} is the matrix operator of the mirror's wave-front responses to electrode voltages:

$$\boldsymbol{\alpha} = \mathbf{M}\mathbf{h}. \quad (8)$$

The elements of \mathbf{M} can therefore be written as

$$M_{jp} = \frac{\partial \alpha_j}{\partial h_p} \quad (9)$$

and measured directly with linear fits to data, where h_p are varied one at a time and $\boldsymbol{\alpha}$ is estimated with PD.

PD data were collected while h_p were stepped one by one through 13 levels while the others were kept at

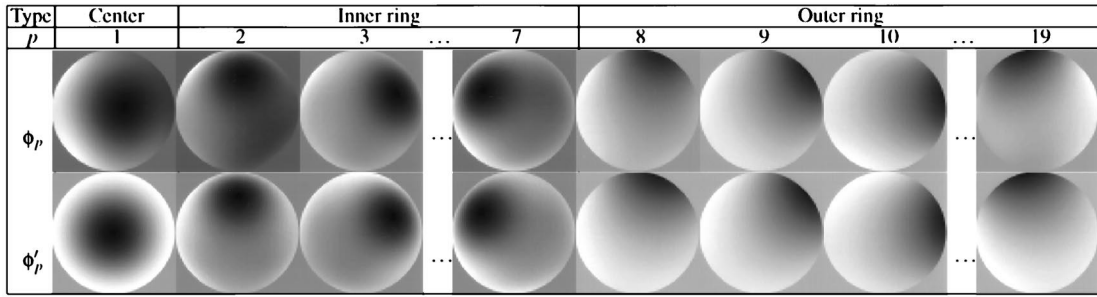


Fig. 3. Sample electrode response wave fronts. Top row, ϕ_p , raw, estimated with PD. Bottom row, ϕ'_p , averaged responses.

zero. For each voltage, fifty 10-ms frames were summed to reduce noise and laboratory seeing. The sequence of voltages was chosen as a coarsely sampled triangle wave, for minimal influence of hysteresis. An average dark frame was subtracted from each image.

In addition to Zernike modes 2–15, we found that Zernike mode 19 also gave a significant response and that active control of this mode was needed to make the mirror flat. It is likely that the mirror can partially correct some higher modes, but, as these cannot be sensed by the SH WFS currently used at the Swedish Vacuum Solar Telescope, we ignored them in these measurements. Wave-front tilts (Zernike modes 2 and 3) shift the image in both PD channels by the same amount, so PD cannot sense them directly. However, the amount of tilt can be inferred from the displacements of the PD-restored pinhole images measured with cross correlation. Note that the observed images cannot be used for this measurement because they will appear as shifted also by, e.g., coma-type aberrations.

A circular pupil $D = 34$ mm was assumed (see the discussion in Section 6 below). All SV's were retained. Note that the noise model in this algorithm is Gaussian additive, which is proper for low-contrast granulation images but not ideal for strong point sources. However, because of the strongly reduced noise from averaging 50 frames, the choice of the actual noise model should not be important. Ultimately, the appropriateness of the algorithm is determined by this procedure's ability to make the mirror flat.

In a preprocessing step, in which the zero-voltage images only were used, the relative registration of the diversity channels was estimated with PD. The corresponding shifts were then adopted as fixed parameters when Zernike coefficients 2–15 and 19 were estimated from the full data set.

Sample electrode response wave-front estimates ϕ_p are shown in Fig. 3. Note that the center and inner ring electrodes produce local curvature within the area of the electrode (cf. Fig. 1) but also tilts that affect the entire pupil area. The electrodes in the outer ring produce strong wave-front tilts that affect the whole pupil.

We estimated the matrix elements M_{jp} by making linear fits to the measured aberration parameters α_j

as a function of the voltage variations v_p . We used only fits that reduced the residual errors v_p by at least 70% to avoid noisy fits from near-zero coefficients. Otherwise the corresponding matrix element was set to zero.

Figure 4 shows graphic representations of the resultant estimated mirror modes \mathbf{v}_j . The electrode maps are scaled individually. In reality, the higher-order modes correspond to higher voltages for unit wave-front rms. When we compare the electrode geometry with the aberrations that they produce it is obvious that there is good overall agreement.

In the electrode voltage maps we can also see variations that do not fit the expected symmetries of the corresponding Zernike polynomials (most easily seen in the symmetrical focus and spherical modes, $m = 4, 11$). The variations are partly real, reflecting gain differences between the electrodes (e.g., from stresses induced by three mirror mounting points, separated by 120°) or misalignment of the pupil to the mirror electrode geometry, and partly the result of uncertainties in the PD estimates. To investigate whether the uncertainties are dominating, we made an alternate set of mirror modes, \mathbf{v}'_j , also shown in Fig. 4. They are based on expansions in Zernike polynomials of the averaged response wave fronts ϕ'_p , examples of which are shown in the bottom tiles in Fig. 3. In ϕ'_p we suppressed deviations from the expected symmetries by replacing each response ϕ_p with the average response in the same ring, taking the different orientations into account. ϕ'_1 , which is alone in the center, is an azimuthal average of ϕ_1 . However, when we used them to calibrate the mirror, \mathbf{v}'_j gave poorer results than \mathbf{v}_j . Thus our tentative conclusion is that a significant part of the variation is real and is not from PD uncertainties. In the following sections we therefore restrict the analysis to the original \mathbf{v}_j modes.

5. Wave-Front Calibration Using a Slow Closed Loop

The most important test of the mirror modes from Section 4—and at the same time of the PD WFS procedure that was used to make them—is whether they can make the wave front flat.

We used PD wave-front sensing with the same parameters as in Section 4 together with control matrix \mathbf{C} to run the mirror in a slow control loop (~ 0.02 Hz, including transfer of data between computers).

j	m	$Z_m = \psi_j$	v_j	v'_j
1	2			
2	3			
3	4			
4	5			
5	6			
6	7			
7	8			
8	9			
9	10			
10	11			
11	12			
12	13			
13	14			
14	15			
15	19			

Fig. 4. Graphic representation of electrode voltages to make Zernike mirror modes. Compare Fig. 1. The electrode maps are scaled individually. White is positive voltage, and black is negative.

100% of the estimated wave fronts were written back to the mirror in each correction. Starting from zero voltages, the loop calibrated the mirror in a few steps from an initial wave-front rms of approximately 0.1 wave to significantly better than the Rayleigh criterion (discussed in Section 6). The main aberrations were astigmatism (~ 0.6 rad), focus (~ 0.3 rad), and coma (~ 0.2 rad).

For the first correction in the loop, seven PD-iterations were needed to reach the convergence criterion. The following corrections, benefitting from

partial correction, needed only three to four iterations.

Figure 5 shows out-of-focus channel image data (defocused images show more wave-front information than in-focus images) along with the corresponding PD estimates for the closed loop. Most of the improvement is in the first two corrections. The difference between the data and the converged estimates is due to aberrations that are not resolved by the corrected modes. The orientation of the hexagonal structure in the second diffraction ring is so well aligned to the horizontal and vertical directions that we suspect that it is caused by stresses from the 120° separated mounts of the mirror. The bump in the first diffraction ring (between 11 and 12 o'clock) could come from the achromat, which is not a high-quality lens. In general, some residual mirror aberrations should be expected as a result of uncorrected mirror modes simply because we are trying to correct a 19-electrode mirror with only 15 modes.

6. Strehl Ratios and Detailed Modeling

We now quantify the results of the calibration. Two well-known quality measures, rms of the wave-front, σ , and Strehl ratio (SR) are used. To measure SR's accurately we need to model the image formation process more carefully than for the PD wave-front sensing used above.

A. Pinhole Modeling

For a qualitative understanding of the modeling we start by looking at pinhole images in the defocused channel. In Fig. 6 we show an aberration-free defocused image, $\tilde{g}_1(0, D)$, where

$$\tilde{g}_k(\alpha, D) = \mathfrak{F}^{-1}\{HS_k(\alpha, D)T(\lambda, \rho)\text{jinc}(\rho R)\}, \quad (10)$$

where $T(\lambda, \rho)$ is a model detector-MTF²⁴ of the KAF 1400 CCD and $\text{jinc}(\rho R)$ is the Fourier transform of a circular pinhole with diameter $2R$ (see, e.g., Ref. 25 or 26), $\text{jinc}(x) = J_1(\pi x)/2x$, and ρ is the radial coordinate in the spatial frequency domain. Note the similarity to the last few PD closed-loop estimates, \hat{g}_1 , in Fig. 5.

The remaining important parameters in the modeling are the wave-front coefficients α . It is evident from Fig. 5 that more parameters than were used in the closed loop are needed to model the morphology of the real data. Figure 7 shows simulations of the real images obtained with the PD wave-front estimates of Zernike coefficients 4–55, where we limited the number of free parameters by setting the number of SV's to 35 in the PD inversions. Because of the low noise in the data used here, we used as H in Eqs. (5) and (10) a fixed circularly symmetrical filter extending to 90% of the diffraction limit. The details in the first and second diffraction rings of the defocused images \tilde{g}_1 in Fig. 5 are well reproduced by the simulated images \tilde{g}_1 .

We now turn to a more quantitative look at the

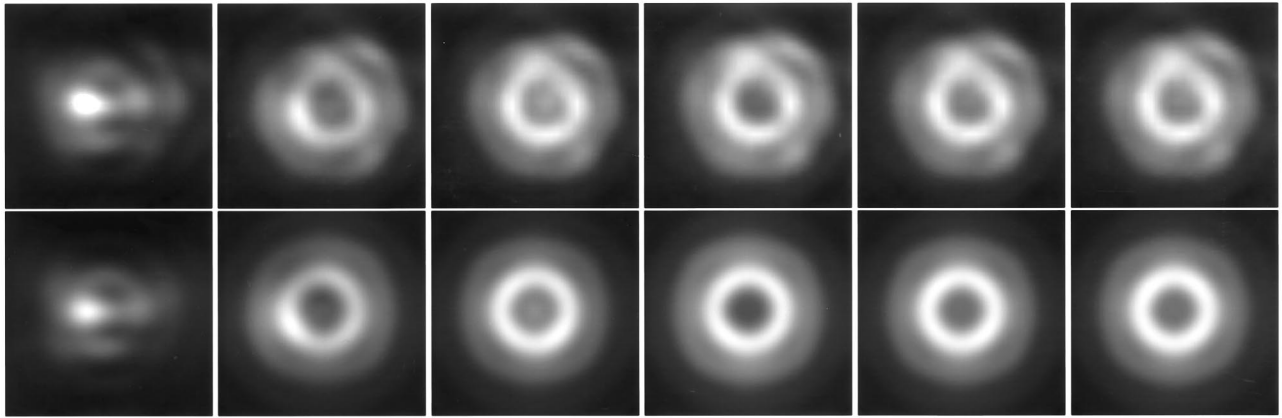


Fig. 5. Out-of-focus images from the closed loop. From the left, 0, 1, . . . , 5 corrections. Top row, observed data, g_1 . Bottom row, corresponding PD estimates, $\tilde{g}_1(\alpha, D)$, with Zernike coefficients 4–15 and 19 and $D = 40$ mm.

closed-loop results, obtained by measurement of SR's in the in-focus channel closed-loop data.

B. Image Strehl Ratio

The most straightforward method of measuring the SR is from the in-focus channel observed images:

$$\mathcal{S}_o = \frac{\text{peak } g_o}{\text{peak } \tilde{g}_o(0, D)}, \quad (11)$$

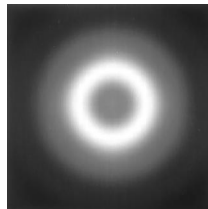


Fig. 6. Simulated aberration-free out-of-focus channel image, $\tilde{g}_1(0, D)$; $D = 33.25$ mm.

where the peak value is a normalized maximum, calculated as

$$\text{peak } g = \frac{\max_x g - b(g)}{\sum_x g - b(g)}. \quad (12)$$

The background level, b , is calculated locally, as an average in a 128×128 pixel frame, outside a 50-pixel radius (approximately seven times the distance to the first diffraction ring). We find that the dark frames alone were not enough to give stable normalization. The subpixel maximum is measured with a two-dimensional quadratic fit to the 5×5 pixel area surrounding the maximum pixel value. The average used for normalization is calculated within a 30-pixel radius. We found these radii after individually adjusting their values until stable estimates of the SR were obtained.

The aberration-free image, $\tilde{g}_o(0, D)$, in the denominator of Eq. (11) needs to be accurately modeled. In particular, we find that \mathcal{S}_o depends critically on D .

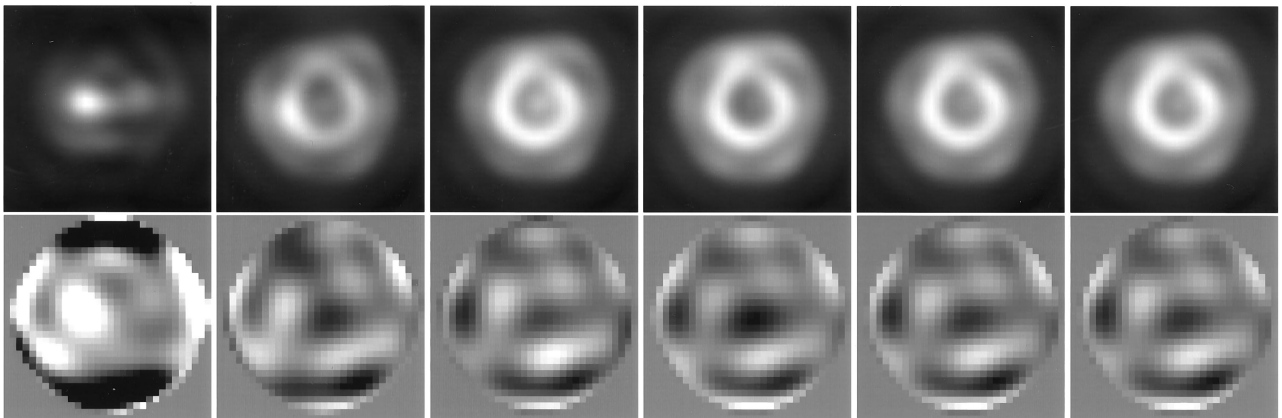


Fig. 7. Top, simulated out-of-focus images, $\tilde{g}_1(\alpha, D)$, corresponding to the closed-loop data. The wave-front coefficients α are PD estimates of Zernike coefficients 4–55 with 35 SV's and $D = 33.25$ mm. Note in particular the excellent agreement with the observed defocused images, g_1 in Fig. 5. Bottom, corresponding wave-front estimates scaled as a set. From the left, 0, 1, . . . , 5 corrections.

The solid line in Fig. 8(a) shows \mathcal{S}_o as a function of D used in making $\tilde{g}_o(0, D)$, which varies by more than 0.025 between 33- and 33.5-mm diameter. This is so because a larger pupil makes a higher aberration-free peak in the denominator and hence a lower SR.

Another potential problem is that \mathcal{S}_o is sensitive to errors in the detector MTF model. Not including the CCD MTF in $\tilde{g}_o(0, D)$ at all reduces \mathcal{S}_o by approximately 0.1 because there is too large a maximum value in the denominator, so this correction is crucial for accurate measurements of the SR. One obvious simplification is that we used a one-dimensional model as a circularly symmetric two-dimensional MTF. The pixel geometry part, which at 633 nm is responsible for more than half of the attenuation at high spatial frequencies, actually has square symmetry.

C. Wave-Front Strehl Ratio

Because we have access to PD data, we can estimate the residual wave fronts by using more parameters than in the closed loop. The SR can then be estimated from the empirical relation

$$\mathcal{S}_\sigma = \exp(-4\pi^2\sigma^2), \quad (13)$$

where σ is the rms of the estimated wave front in waves. When $\mathcal{S}_\sigma > 0.90$, this approximation should give essentially zero error for the primary aberrations.²⁷

The measured σ depends on the wave-front parameterization used in the PD inversion. Figure 8(b) shows \mathcal{S}_σ after five corrections as a function of the number of SV's used in estimating interchannel registration and Zernike coefficients 4–55. There is a plateau between approximately 30 and 45 SV's, and then σ drops. We interpret this result as follows: The wave front is fully resolved by approximately 30 parameters. The PD problem turns nearly singular with approximately 45 SV's, which gives increasing σ because of errors in the inversions.

Figure 8(a) shows that $\mathcal{S}_\sigma \approx 0.970$ for 35 SV's, on the other hand, is almost constant over the interval, so it is not so sensitive as \mathcal{S}_o to the pupil diameter. The two curves cross at $D = 33.4$ mm, almost exactly the average measured diameter.

We show the estimated wave fronts in Fig. 7. The rms of the estimated wave front for $D = 33.25$ mm, Zernike coefficients 4–55, and 35 SV's is $\sigma = 0.027$ wave. Almost all the residual wave front comes from uncorrected modes 16–18 and 20–55; $\sigma_{\text{uncorr}} = 0.026$ wave. The corrected modes contribute with $\sigma_{\text{corr}} = 0.008$ wave. The four largest residuals measured are, in order, Zernike modes 37, 42, 48, and 49. Zernike mode 37 is circularly symmetrical, and the others are 60 and 30 modes. This indicates that we really did have problems with the pupil diameter and perhaps that effects from the 120° supports are not fully compensated for.

Whatever the source, model mismatches can be mistaken for aberrations by PD, most likely leading to overestimated σ because PD needs some extra ab-

errations to compensate for the mismatch. Therefore \mathcal{S}_σ serves as a lower limit of the SR. It is possible that better estimates of σ (and therefore of \mathcal{S}_σ) may be possible in the future with a new PD algorithm that is based on minimizing the error in the wave front directly.⁸

D. Simulated-Image Strehl Ratio

The effects on \tilde{g}_o of minor model mismatch in the pupil geometry (D) or in the model MTF cancel if they appear in both the numerator and the denominator of the SR expression. We therefore define

$$\mathcal{S}_s = \frac{\text{peak } \tilde{g}_o(\alpha, D)}{\text{peak } \tilde{g}_o(0, D)}, \quad (14)$$

where, unlike in Eq. (11), the aberrated image in the numerator also is simulated, by use of the PD wave-front estimate.

Figures 8(b) and 8(a), respectively, show how \mathcal{S}_s depends on the wave-front parameterization and the pupil diameter. In essence, it behaves as \mathcal{S}_σ but at a slightly higher level. As functions of D , S_s and \mathcal{S}_o cross near $D = 33.25$ mm, where the SR is ~ 0.977 .

\mathcal{S}_s does not drop as fast as \mathcal{S}_σ at large SV's. We conjecture that this is so because of null-space contributions to the wave front that do not affect the modeled images as much as they increase σ .

Model mismatches cancel, but errors in the wave front affect \mathcal{S}_s , because $\tilde{g}_o(\alpha, D)$ then only partially compensates for aberrations. This would tend to give a too blurry image in the numerator, with too small a peak value. So, like \mathcal{S}_σ , \mathcal{S}_s would tend to underestimate the true SR, although the accuracy should be better because the full wave-front information, not only the rms, is used.

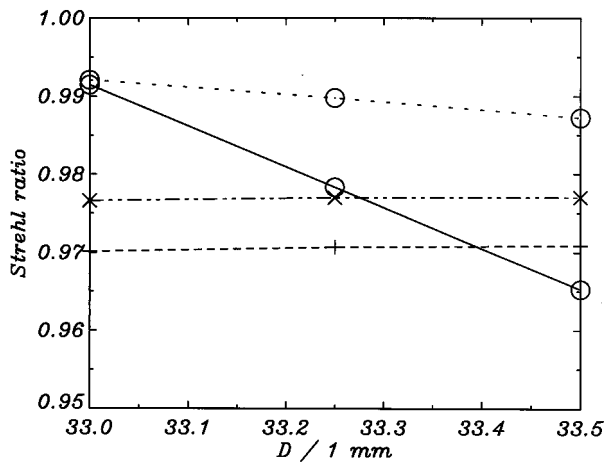
E. PD-Object Strehl Ratios

So far, we have three different definitions of the SR, one model-dependent calculation and two underestimates. A way to avoid the model dependencies is to use the PD object estimate \hat{f} , which includes information on the pinhole size from the image data. Because the detector MTF, T , affects both image channels in the same way, an estimate of T is automatically included in \hat{f} . So we can make simulated images by using \hat{f} and Eq. (4) rather than jinc and T as in Eq. (10). With these images, we can define two additional SR's:

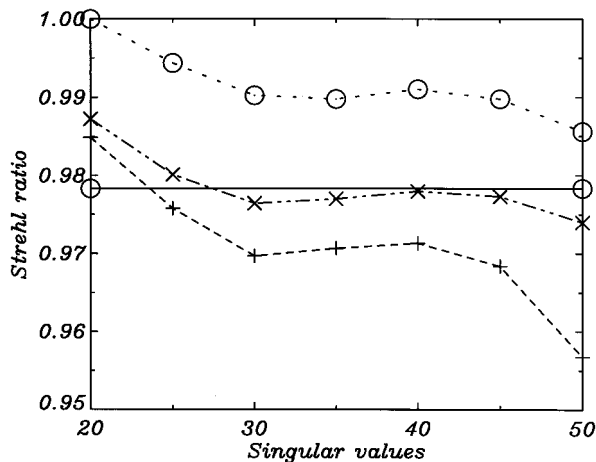
$$\mathcal{S}_{\text{OPD}} = \frac{\text{peak } g_0}{\text{peak } \hat{g}_o(0, D)}, \quad (15)$$

$$\mathcal{S}_{\text{SPD}} = \frac{\text{peak } \hat{g}_o(\alpha, D)}{\text{peak } \hat{g}_o(0, D)}, \quad (16)$$

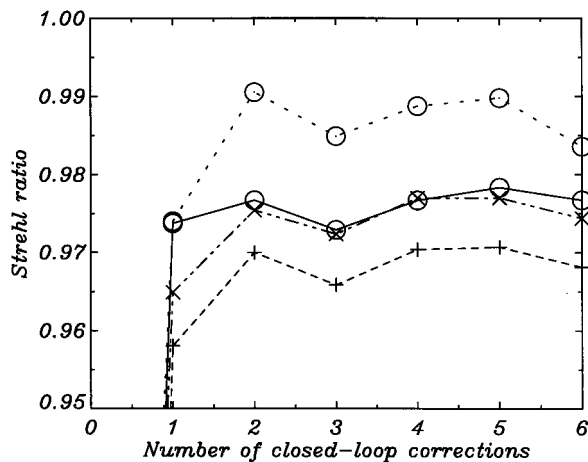
similar to \mathcal{S}_o in Eq. (11) and \mathcal{S}_s in Eq. (14), respectively. Note that it is the error in \hat{g}_k that is minimized, rather than that in either \hat{f} or \hat{s}_k [see Eq. (3)], and we have previous experience to suggest that the algorithm prefers to give wave-front errors rather than object errors.⁴



(a)



(b)



(c)

Fig. 8. SR's from closed-loop data: (a) after 5 corrections, for 35 SV's as a function of pupil diameter D ; (b) after 5 corrections, for $D = 33.25$ mm as a function of the number of SV's; (c) for $D = 33.25$ mm and 35 SV's, as a function of the number of corrections. Solid lines, measured directly from observed images (\mathcal{S}_o); dashed-dotted-dotted lines, measured from simulated images (\mathcal{S}_s); dashed lines, from wave-front rms (\mathcal{S}_σ); dotted lines, observed images and PD object in the denominator (\mathcal{S}_{OPD}). The circles group the two observed image SR's, \mathcal{S}_o and \mathcal{S}_{OPD} , together. Note that in (b) SV's do not enter into the calculation of the constant \mathcal{S}_σ .

Figure 8 shows that \mathcal{S}_{OPD} yields the largest SR estimates. Indeed, \mathcal{S}_{OPD} should be an overestimation of SR, because errors in \hat{f} owing to wave-front trade-offs would tend to make the peak value in the denominator smaller, much as \mathcal{S}_σ and \mathcal{S}_s are underestimated. Thus we have bracketed the true SR.

If the expressions for \hat{g}_k and \tilde{g}_k are compatible, we expect that $\mathcal{S}_{SPD} \equiv \mathcal{S}_S$. Our data pass this sanity check, because the equivalence holds to within less than 0.001. To avoid cluttering the diagram, we do not show \mathcal{S}_{SPD} in Fig. 8.

F. Scanned Pupil Mask

The average measured pupil diameter agrees well with the most likely D from the comparison of several SR measurements. However, the effect of deviations from a circular shape needs to be investigated. We calculated \mathcal{S}_{OPD} and \mathcal{S}_o with eight different orientations of a scanned pupil mask, scaled to approximately the correct size.

The variations in \mathcal{S}_{OPD} are less than ± 0.001 ; in \mathcal{S}_o they are even smaller, $\ll 0.001$. We conclude that this is not a significant source of error.

7. Conclusions

From the consistency of all the SR measurements, adopting \mathcal{S}_σ as a lower limit and disregarding \mathcal{S}_{OPD} , we conclude that we have measured the SR of the converged closed-loop images to 0.975 ± 0.005 . This corresponds to a wave-front rms of $1/(40 \pm 4)$ wave, or 0.025 ± 0.0025 wave at 633 nm. This is of the order of the $\lambda/10$ PTV guaranteed by Laplacian Optics, Inc., and much better than the Rayleigh $\lambda/4$ PTV wave-front criterion, corresponding to a $\lambda/14$ rms wave front for smooth wave-front deformation or $\lambda/20$ when higher-order aberrations are dominating.²⁸

These SR measurements are actually conservative values as far as the mirror quality goes, in part because the PD closed loop suffered from the erroneous assumption of a 34-mm pupil. It is likely that better calibration is possible with correct pupil representation in the loop PD inversions. Also, it is likely that at least part of the residual aberrations comes from the 1525-mm lens that is used in double pass.

The conclusion is that, with PD, the mirror can be well calibrated. One advantage of PD calibration with respect to calibration with an external WFS is the simple optical setup, including the ability to use extended objects. Another is that the wave front can be calibrated at the image plane of the science camera itself, therefore involving also any reimaging optics.

Wave-front sensing in the science cameras can also be used as a tool for calibrating an external WFS, such as a SH WFS, with the aberration differences between the optical paths of the SH WFS and the science camera taken into account.

For some applications (see, e.g., Ref. 5) the PD setup does not require any extra optics, because the science cameras are equipped with a PD beam splitter anyway, to compensate for residual wave fronts in postprocessing. If PD wave-front information is not

required, it is easy to remove the PD beam splitter when one is recording science data.

The PD technique described here has potential for improvement. There is noise in the control matrix, partly because the object is estimated independently for each voltage applied to the mirror. In joint phase diverse speckle^{9,29} (JPDS) a single object is estimated from several pairs of PD frames. This makes the optimization algorithm less likely to trade errors between the joint object and the individual wave fronts. In particular, JPDS forces changes in voltages to be interpreted as changes in the wave front, not in the object. For measurements of the control matrix, JPDS should therefore improve the accuracy. We are currently working on an extension of our linearized algorithm to handle JPDS also. Also, when the object is simple and known (e.g., a circular pinhole of known size as in our setup or an unresolved star or one with a known size), PD data can be analyzed with a modeled object, preventing any object-wave-front trade-offs by using a special case of phase diversity processing referred to as phase-diverse phase retrieval.^{11,17,30} However, any errors in the modeled object may still give systematic errors in the wave-front estimates.

We thank Laplacian Optics, Inc., for its efforts in producing an excellent mirror and also for providing Fig. 1. The analog-to-digital converter that connects the computer to the high-voltage amplifier was made by workshop personnel at the Kiepenheuer-Institut für Sonnenphysik in Freiburg, Germany. Eric Stevens of the Eastman Kodak Company calculated the model detector MTF for the KAF-1400 CCD. Henrik Blomberg assisted with the optical setup and made Fig. 2. Göran Hosinsky carefully scanned and measured the dimensions of the pupil mask.

References

1. G. B. Scharmer, D. S. Brown, L. Pettersson, and J. Rehn, "Concepts for the Swedish 50-cm Vacuum Solar Telescope," *Appl. Opt.* **24**, 2558–2564 (1985).
2. M. Shand and G. Scharmer, "The Swedish Vacuum Solar Telescope data acquisition and control systems," in *Site Properties of the Canarian Observatories*, C. Muñoz-Tuñón, ed., Vol. 42 of *New Astronomy Reviews* (Elsevier, Amsterdam, 1998), pp. 481–484.
3. M. Shand, G. B. Scharmer, and W. Wei, "Correlation tracking and adaptive optics control using off-the-shelf workstation technology," in *High Resolution Solar Physics: Theory, Observations and Techniques*, T. Rimmele, R. R. Radick, and K. S. Balasubramaniam, eds., *Proceedings of the Nineteenth Sacramento Peak Summer Workshop*, Vol. 183 of the *Astronomical Society of the Pacific Conference Series* (ASP, San Francisco, Calif., 1999), p. 231.
4. M. G. Löfdahl and G. B. Scharmer, "Wavefront sensing and image restoration from focused and defocused solar images," *Astron. Astrophys. Suppl. Ser.* **107**, 243–264 (1994).
5. M. G. Löfdahl, T. E. Berger, R. A. Shine, and A. M. Title, "Preparation of a dual wave-length sequence of high-resolution solar photospheric images using phase diversity," *Astrophys. J.* **495**, 965–972 (1998).
6. G. B. Scharmer, M. Owner-Petersen, T. Korhonen, and A. Title, "The new Swedish solar telescope," in *High Resolution Solar Physics: Theory, Observations and Techniques*, T. Rimmele, R. R. Radick, and K. S. Balasubramaniam, eds., *Proceedings of the Nineteenth Sacramento Peak Summer Workshop*, Vol. 183 of the *Astronomical Society of the Pacific Conference Series* (ASP, San Francisco, Calif., 1999), p. 157.
7. G. B. Scharmer, M. Shand, M. G. Löfdahl, and W. Wei are preparing a manuscript to be called "A workstation based solar adaptive optics system."
8. G. B. Scharmer, "Object-independent fast phase-diversity," in *High Resolution Solar Physics: Theory, Observations and Techniques*, T. Rimmele, R. R. Radick, and K. S. Balasubramaniam, eds., *Proceedings of the Nineteenth Sacramento Peak Summer Workshop*, Vol. 183 of the *Astronomical Society of the Pacific Conference Series* (ASP, San Francisco, Calif., 1999), p. 330.
9. R. G. Paxman, J. H. Seldin, M. G. Löfdahl, G. B. Scharmer, and C. U. Keller, "Evaluation of phase-diverse techniques for solar-image restoration," *Astrophys. J.* **466**, 1087–1099 (1996).
10. R. L. Kendrick, D. S. Acton, and A. L. Duncan, "Phase-diversity wave-front sensor for imaging systems," *Appl. Opt.* **33**, 6533–6546 (1994).
11. R. G. Paxman, T. J. Schulz, and J. R. Fienup, "Joint estimation of object and aberrations by using phase diversity," *J. Opt. Soc. Am. A* **9**, 1072–1085 (1992).
12. R. G. Paxman and J. R. Fienup, "Optical misalignment sensing and image reconstruction using phase diversity," *J. Opt. Soc. Am. A* **5**, 914–923 (1988).
13. R. A. Gonsalves and R. Chidlaw, "Wavefront sensing by phase retrieval," in *Applications of Digital Image Processing III*, A. G. Tescher, ed., *Proc. SPIE* **207**, 32–39 (1979).
14. M. G. Löfdahl, A. L. Duncan, and G. B. Scharmer, "Fast phase diversity wavefront sensing for mirror control," in *Adaptive Optical System Technologies*, D. Bonnaccini and R. K. Tyson, eds., *Proc. SPIE* **3353**, 952–963 (1998).
15. R. G. Paxman and J. H. Seldin, "Fine-resolution astronomical imaging with phase-diverse speckle," in *Digital Recovery and Synthesis II*, P. S. Idell, ed., *Proc. SPIE* **2029**, 287–298 (1993).
16. R. L. Kendrick, R. Bell, A. L. Duncan, G. D. Love, and D. S. Acton, "Closed loop wavefront correction using phase diversity," in *Space Telescopes and Instruments V*, P. Y. Bely and J. B. Breckinridge, eds., *Proc. SPIE* **3356**, 844–853 (1998).
17. M. G. Löfdahl, R. L. Kendrick, A. Harwit, K. E. Mitchell, A. L. Duncan, J. H. Seldin, R. G. Paxman, and D. S. Acton, "A phase diversity experiment to measure piston misalignment on the segmented primary mirror of the Keck II telescope," in *Space Telescopes and Instruments V*, P. Y. Bely and J. B. Breckinridge, eds., *Proc. SPIE* **3356**, 1190–1201 (1998).
18. D. J. Lee, B. M. Welsh, M. C. Roggemann, and B. L. Ellerbroek, "Diagnosing unknown aberrations in an adaptive optics system by use of phase diversity," *Opt. Lett.* **22**, 952–954 (1997).
19. R. J. Noll, "Zernike polynomials and atmospheric turbulence," *J. Opt. Soc. Am.* **66**, 207–211 (1976).
20. C. L. Lawson and R. J. Hanson, *Solving Least Squares Problems* (Prentice-Hall, Englewood Cliffs, N.J., 1974).
21. W. H. Press, S. A. Teukolsky, W. T. Vetterling, and B. P. Flannery, *Numerical Recipes in C, The Art of Scientific Computing*, 2nd ed. (Cambridge U. Press, Cambridge, UK, 1992).
22. M. J. Northcott, Laplacian Optics, Inc., Suite 134, 2800 Woodlawn Drive, Honolulu, HI 96822 (personal communication, 1999).
23. F. Roddier, "The problematic of adaptive optics design," in *Adaptive Optics for Astronomy*, D. M. Alloin and J.-M. Mariotti, eds., *NATO ASI Series* **423**, 89–112 (1994).
24. E. G. Stevens and J. P. Lavine, "An analytical, aperture, and two-layer carrier diffusion MTF and quantum efficiency model for solid-state image sensors," *IEEE Trans. Electron. Dev.* **41**, 1753–1760 (1994).

25. J. W. Goodman, *Introduction to Fourier Optics*, 2nd ed. (McGraw-Hill, New York, 1996).
26. R. N. Bracewell, *Two-Dimensional Imaging* (Prentice-Hall, Englewood Cliffs, N.J., 1995).
27. V. N. Mahajan, "Strehl ratio for primary aberrations: some analytical results for circular and annular pupils," *J. Opt. Soc. Am.* **72**, 1258–1266 (1982).
28. W. J. Smith, *Modern Optical Engineering: The Design of Optical Systems*, 2nd ed. (McGraw-Hill, New York, 1990).
29. R. G. Paxman, T. J. Schulz, and J. R. Fienup, "Phase-diverse speckle interferometry," in *Signal Recovery and Synthesis IV*, Vol. 11 of 1992 OSA Technical Digest Series (Optical Society of America, Washington, D.C., 1989), pp. 5–7.
30. B. L. Ellerbroek, B. J. Thelen, D. J. Lee, D. A. Carrara, and R. G. Paxman, "Comparison of Shack–Hartmann wavefront sensing and phase-diverse phase retrieval," in *Adaptive Optics and Applications*, R. K. Tyson and R. Q. Fugate, eds., Proc. SPIE **3126**, 307–320 (1997).